Response of the West African Monsoon to the Madden–Julian Oscillation

SALLY L. LAVENDER

School of Environmental Sciences, University of East Anglia, Norwich, United Kingdom

ADRIAN J. MATTHEWS

School of Environmental Sciences, and School of Mathematics, University of East Anglia, Norwich, United Kingdom

ABSTRACT

Observations show that rainfall over West Africa is influenced by the Madden–Julian oscillation (MJO). A number of mechanisms have been suggested: 1) forcing by equatorial waves; 2) enhanced monsoon moisture supply; and 3) increased African easterly wave (AEW) activity. However, previous observational studies are not able to unambiguously distinguish between cause and effect. Carefully designed model experiments are used to assess these mechanisms. Intraseasonal convective anomalies over West Africa during the summer monsoon season are simulated in an atmosphere-only global circulation model as a response to imposed sea surface temperature (SST) anomalies associated with the MJO over the equatorial warm pool region. 1) Negative SST anomalies stabilize the atmosphere leading to locally reduced convection. The reduced convection leads to negative midtropospheric latent heating anomalies that force dry equatorial waves. These waves propagate eastward (Kelvin wave) and westward (Rossby wave), reaching Africa approximately 10 days later. The associated negative temperature anomalies act to destabilize the atmosphere, resulting in enhanced monsoon convection over West and central Africa. The Rossby waves are found to be the most important component, with associated westward-propagating convective anomalies over West Africa. The eastward-propagating equatorial Kelvin wave also efficiently triggers convection over the eastern Pacific and Central America, consistent with observations. 2) An increase in boundary layer moisture is found to occur as a result of the forced convective anomalies over West Africa rather than a cause. 3) Increased shear on the African easterly jet, leading to increased AEW activity, is also found to occur as a result of the forced convective anomalies in the model.

1. Introduction

The West African region receives almost all its annual rainfall during the monsoon season. The West African monsoon (WAM) is highly variable on decadal, annual, and intraseasonal time scales (e.g., Lebel et al. 2000). There are a number of external and internal forcings on this monsoon system including sea surface temperature (Folland et al. 1986; Rowell et al. 1995; Janicot et al. 1998), land–atmosphere feedbacks (Taylor et al. 1997; Grodsky and Carton 2001; Douville 2002), and large-scale circulation features (Matthews 2004a; Mounier et al. 2007). General circulation models (GCMs) tend to poorly simulate the WAM climate and its variability (Sperber and Palmer 1996). This poor forecasting skill

was shown during the JET2000 experiment (Thorncroft et al. 2003). The errors appear to be systematic and so are of global importance since, although the convection processes are unusually dominant in the region, they are not unique to Africa.

The WAM is a land–ocean–atmosphere-driven system, influenced by two air masses that meet in the intertropical convergence zone (ITCZ). The northeasterly trade winds, referred to as Harmattan winds, originate from the Sahara Desert and contain warm, dry air that is generally dusty. The lower boundary of this air mass slopes upward to the south over the southwesterly monsoon flow carrying cooler, humid tropical maritime air originating over the Atlantic. The seasonal migration of this convergence zone controls the annual monsoons and rainfall; understanding of this migration is vital for understanding the climate of West Africa.

On the intraseasonal time scale there is high day-to-day variability in rainfall, most likely linked to the passing

Corresponding author address: Sally Lavender, School of Earth Sciences, University of Melbourne, Parkville, VIC 3010, Australia.
E-mail: sallyl@unimelb.edu.au

of African easterly waves (AEWs; Diedhou et al. 1999; Gu et al. 2004) and mesoscale convective systems (MCSs; Mathon et al. 2002), but on a longer time scale there are prolonged wet and dry events during the monsoon season (Janicot and Sultan 2001). These periods can be devastating to crop yields in a region that has a history of droughts and famine. Hence, there has been considerable interest in the intraseasonal variability of the WAM during recent years. There are two dominant frequency bands for the intraseasonal modulation of convection in the WAM, one with a period of around 15 days and the other within the 25–60-day band (Sultan et al. 2003). There is no clear conclusion to the mechanism controlling the occurrence of this variability. The shorter time-scale variability may be linked to fluctuations in the advection of moisture from over the Atlantic to the Sahel (Mounier and Janicot 2004), which may be associated with the quasi-biweekly zonal dipole (Mounier et al. 2008). The longer time-scale variability is now thought to be associated with the Madden–Julian oscillation (MJO; Matthews 2004a) and associated intraseasonal variability of the Asian summer monsoon (Janicot et al. 2009).

The MJO is the dominant component of intraseasonal variability on the global scale (Madden and Julian 1994; Zhang 2005). This oscillation has a period of 30–90 days with an average eastward propagation speed of 5 m s^{-1}. The MJO is first evident over the west Indian Ocean with the development of a low surface pressure anomaly; this is accompanied by enhanced boundary layer convergence and an increase in convection and precipitation. The MJO then propagates eastward over the warm western Pacific where it reaches its maximum intensity and over the cooler central Pacific when the convective anomalies appear to dissipate, reappearing over the warmer tropical Atlantic and Indian Ocean. Sea surface temperatures (SSTs) have been shown to be important in forcing the convection associated with the MJO (Woolnough et al. 2001; Matthews 2004b; Klingaman et al. 2008), suggesting that the MJO is at least a partially coupled atmosphere–ocean phenomenon (e.g., Sperber et al. 1997). Positive (negative) SST anomalies tend to lead the maximum (minimum) in convection by approximately 10–12 days.

Matthews (2004a) used reanalysis and satellite data to determine the structure of the dominant mode of intraseasonal variability of the WAM, finding that this is at least partly due to the MJO. Twenty days before enhanced convection over Africa, there was an MJO-associated region of reduced convection over the equatorial warm pool. This forced equatorial Kelvin and Rossby waves, which propagated eastward and westward, respectively, away from the forcing region. These

waves met up 20 days later over Africa where their negative midtropospheric temperature anomalies acted to destabilize the atmosphere, resulting in deep convection over Africa. These results have been supported using precipitation data (Maloney and Shaman 2008). Janicot et al. (2009) also found the MJO to be important in controlling the variability of the WAM and additionally found a westward propagating mode of variability over West Africa that was linked to the Indian monsoon. Based on these results, the MJO is thought to partly explain the 25–60-day mode of intraseasonal variability over West Africa. However, observational analyses can only reveal statistical inferences of associations and lead to hypotheses. They cannot be used on their own to unambiguously determine cause and effect. Hence, the hypothesis that the MJO forces the WAM is tested in this paper in a numerical experiment using a GCM.

This paper builds on the work of Matthews (2004a) and aims to examine if variability in the WAM can be forced as a response to the MJO. Carefully designed experiments with a GCM are used to simulate convection over West Africa when forced with SST anomalies associated with the MJO. Three mechanisms have been suggested and will be analyzed using the model results: 1) the forcing by equatorial waves, 2) enhanced monsoon moisture supply, and 3) increased AEW activity. Details of the data and model are given in section 2. Observational results are analyzed in section 3. The forcing of the model is described in section 4, and modeled results are analyzed in section 5. Finally, conclusions are presented in section 6.

2. Data

Outgoing longwave radiation (OLR) is used as a proxy for deep convection and rainfall in the tropics (e.g., Arkin and Ardanuy 1989) owing to high, cold cloud tops resulting in low values of OLR. Daily mean OLR satellite data on a 2.5° × 2.5° grid were obtained for the years 1982–2005, from the National Oceanic and Atmospheric Administration. These had been interpolated to remove any missing data (Liebmann and Smith 1996).

Sea surface temperature data were available from the NOAA optimum interpolation version 2 (OIv2) SST analysis dataset from 1982 to 2005 (Reynolds et al. 2002). The data were available on a 1° × 1° grid as weekly means and were interpolated to daily values. The 7-day sampling is sufficient to capture intraseasonal variability. However, it would not be able to accurately capture higher frequency SST variability.

Daily Microwave Sounding Unit (MSU) temperature data were available on a 2.5° × 2.5° grid for the years

1979–93. The upper-tropospheric temperature is taken from a combination of channels 3 and 4 (MSU34) with a peak in signal at 250 hPa and most of its signal originating between 500 and 100 hPa.

To obtain the intraseasonal anomalies, the first five harmonics of the annual cycle were removed from each dataset. These were then passed through a 10–200-day bandpass Lanczos filter (Duchon 1979), so only variability on the time scales of interest is included.

3. Observed MJO link with West Africa

Matthews (2004a) found that, by creating regression maps based on the dominant mode of convection (OLR) over West Africa, there was a link with the OLR over the equatorial warm pool 20 days previously. By analyzing the midtropospheric temperature anomalies it was suggested that dry equatorial Kelvin and Rossby waves are forced by the cool midtropospheric temperatures due to the suppressed convection over the warm pool. These waves then propagate around the globe, meeting over West Africa where their associated negative temperature anomalies act to destabilize the atmosphere, resulting in convection. Two other mechanisms were suggested that were associated with this equatorial wave propagation. First, the low-level westerly anomalies associated with the Kelvin wave increased the monsoon flow and moisture supply to the region. Second, these westerly anomalies may also act to increase the horizontal shear on the African easterly jet (AEJ), causing it to become more barotropically unstable. This may lead to enhanced African easterly waves and convective activity.

This observed link between the MJO and the WAM is examined further here. First, a similar analysis to that performed by Matthews (2004a) was carried out; this will later be compared to the modeled results. An empirical orthogonal function (EOF) analysis of the intraseasonal 10–200-day filtered satellite OLR anomalies, during the June–September monsoon season, was performed on a domain centered on the West African region (10°S–20°N, 40°W–40°E). The leading eigenvector (EOF1) accounted for 16.8% of the variance and was well separated from the next eigenvector (EOF2: 10.3% of the variance) according to the criteria of North et al. (1982). EOF2 was separated from the remaining eigenvectors, which formed a degenerate set. This analysis was repeated using a larger domain to confirm that it was not domain dependent (Richman 1986). A lag correlation showed that the principal component time series of EOF1 and EOF2 were uncorrelated at the 95% significance level. Hence, EOF2 will not be considered further. The dominant mode of intraseasonal variability
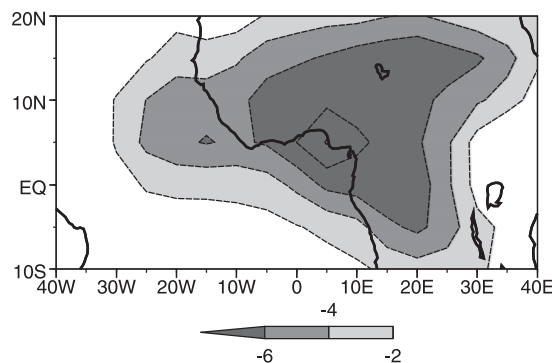

FIG. 1. EOF1 of 10–200-day filtered satellite OLR over West Africa (10°S–20°N, 40°W–40°E) for June–September from 1983 to 2005: contour interval is 2 W m^{-2}; the zero contour is omitted and negative contours are dashed; shading is shown by the legend.

over West Africa (EOF1, Fig. 1) is a large region of negative OLR anomalies (enhanced convection). As found by Matthews (2004a), there are two regions of anomalies, one along 10°–15°N and another southeastward-oriented region over central Africa.

Time-lagged composites were produced based on when the first principal component (PC) time series was a maximum and above a threshold of one standard deviation (60 cases). Hence, day 0 in the lagged composites (Fig. 2c) corresponds to the time when PC1 is a maximum. Over West Africa this looks very similar to EOF1 (Fig. 1). On day 0 (Fig. 2c) there are also convective anomalies elsewhere over the tropics. There is reduced convection north of the equator between 60°E and 150°W and enhanced convection over the equatorial Indian Ocean and western Pacific. Twenty days before the convection over West Africa peaks (day −20, Fig. 2a) there is enhanced convection north of the equator between 90°E and 150°W and reduced convection over the western Indian Ocean. There is also suppressed convection over the Gulf of Guinea. Ten days later (day 10, Fig. 2b) there is a region of reduced convection over the Indian Ocean, extending over Indonesia and the western Pacific, with enhanced convection over Central America. The region of suppressed convection on day −10 has propagated northeastwards and decayed slightly by day 0 (Fig. 2c) when the maximum in convection occurs over West Africa. On day 10 (Fig. 2d) the sign of the warm pool anomalies are reversed with enhanced convection over the Indian Ocean and Indonesia. There is also reduced convection over Central America. A northeastward propagation of the suppressed convection can be seen from 0°, 60°E on day −20 (Fig. 2a) to 5°N, 90°–120°E on day −10 (Fig. 2b) and to 10°N, 60°E–150°W on day 0 (Fig. 2c). The northeastward propagation of the convective anomalies
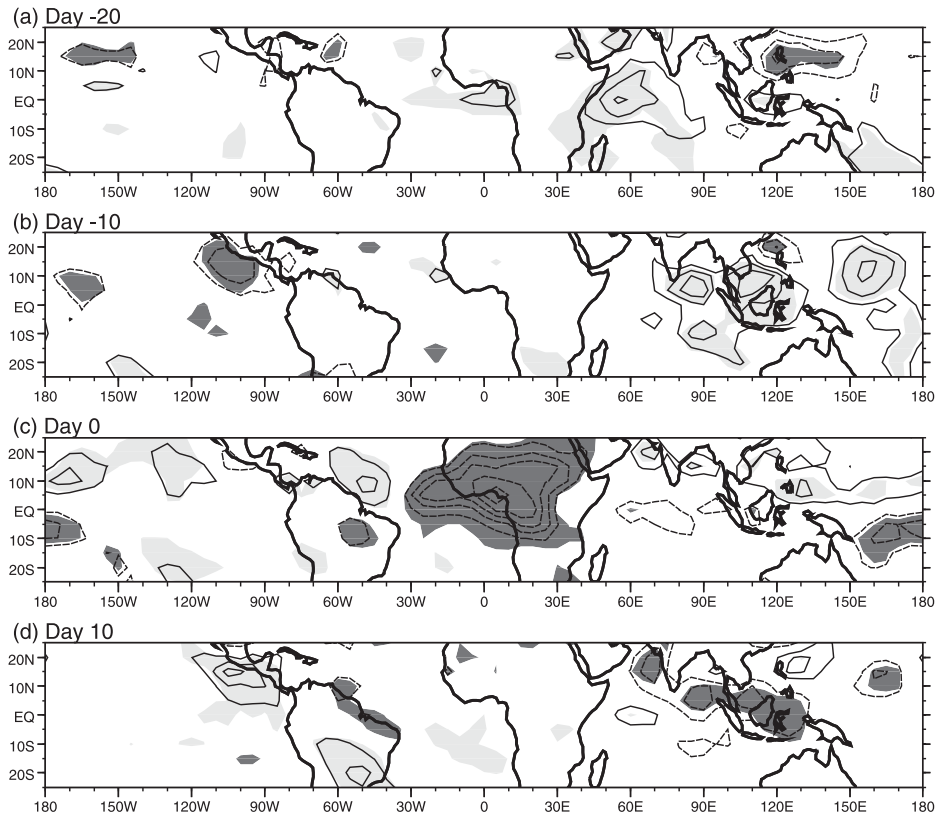
FIG. 2. Lagged composite maps of satellite OLR anomalies based on PC1 of 10–200-day filtered OLR over West Africa for June–September from 1983 to 2005 on days (a) −20, (b) −10, (c) 0, and (d) 10: contour interval is 3 W m^{-2}, negative contours are dashed, and the zero contour is omitted. Shading indicates the values significant at the 95% level.

over the warm pool is similar to those of the MJO during northern summer (Wheeler and Hendon 2004; Annamalai and Slingo 2001), as suggested by Matthews (2004a).

Based on analysis of a number of variables, one of the mechanisms suggested by Matthews (2004a) was that "cold" equatorial Kelvin and Rossby waves are forced by the negative latent heating anomaly associated with the suppressed convection over the warm pool. The dry Kelvin wave propagates eastward, and the Rossby wave westward around the globe and meet over Africa where their associated negative midtropospheric temperature anomalies act to destabilize the atmosphere, resulting in an enhancement of convection. Such propagation can be seen in the Hovmöller diagram of MSU34 temperature and OLR anomalies, averaged between 10°S and 10°N (Fig. 3). The peak signal in temperature starts from approximately 150°E on day −5, associated with suppressed convection a few days previously. The eastward-propagating signal (with a structure consistent with an equatorial Kelvin wave, not shown) has an average speed of 31 m s^{-1}. The westward-propagating

signal has a structure associated with an equatorial Rossby wave (not shown) and propagates at 21 m s^{-1}. The two signals meet at 5°E on day 2 when there is enhanced convection. As found by Matthews (2004a), the ratio of Kelvin to Rossby wave speeds is smaller than those predicted by linear wave theory (1.5 rather than 3, Matsuno 1966; Gill 1980), as there are a number of other factors such as basic-state wind and interaction with convection and orography that are not included in the simple linear model.

The analysis discussed above and by Matthews (2004a) is based on the dominant convective mode over West Africa and finds a possible link with the MJO. To test the robustness of this relationship the analysis is turned around and will be based on the MJO itself to see if this is linked with a remote signal over West Africa. An EOF analysis was performed over the warm pool region (25°S–25°N, 40°E–120°W) on the 10–200-day filtered intraseasonal satellite OLR anomalies over the full years from 1983 to 2004. The leading eigenvector accounts for 7.4% of the variance and is significantly separated from the second eigenvector, which accounts
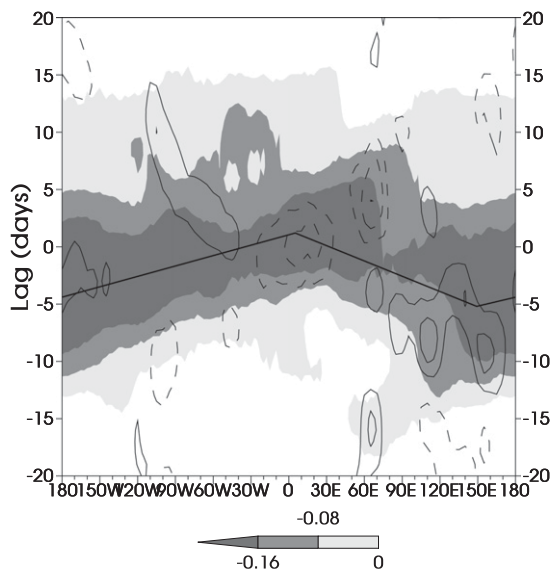
FIG. 3. Hovmöller diagram of lagged equatorial MSU34 mid-tropospheric temperature anomalies (shading) averaged between 10°S and 10°N and OLR anomalies (contours) averaged between 5°N and 15°N, based on PC1 of 10–200-day filtered OLR over West Africa: OLR contour interval is 5 W m^{-2}, negative contours are dashed and the zero contour is omitted; shading is shown by the legend. The thick straight line highlights the propagation of the peak temperature anomalies.

for 5.8%, according to the criteria of North et al. (1982). The second eigenvector is in turn significantly separated from the third (4.2%). The first EOF (Fig. 4a) shows enhanced convection associated with negative OLR anomalies over the Indian Ocean and a region of reduced convection over the western Pacific. The second EOF (Fig. 4b) shows a large region of enhanced convection over Indonesia with reduced convection over the South Pacific. PC1 and PC2 were found to be significantly lag-correlated at the 95% level with PC1 leading PC2 by approximately 11 days, a quarter of a MJO cycle. This means that, 11 days after OLR anomalies as seen in EOF1 are present, those seen in EOF2 will occur, forming eastward propagating anomalies. Consistent with many previous studies (e.g., Hendon and Salby 1994; Matthews 2000), these leading two EOFs describe and define the MJO.

The MJO can be represented by a vector in two-dimensional phase space with an amplitude of $A(t) = [\text{PC1}^2(t) + \text{PC2}^2(t)]^{1/2}$ and a phase of $\alpha(t) = \tan^{-1}[\text{PC2}(t)/\text{PC1}(t)]$ (Matthews 2000; Wheeler and Hendon 2004). The eastward propagation will be associated with an increase in phase (α) with time (t), that is, a counterclockwise rotation about the origin (Fig. 5).

To produce a composite cycle, the MJO (in phase space) is divided into eight categories, shown in Fig. 5. Each day is assigned to a particular category depending

on its phase and amplitude. Only days within the months June–September (JJAS) and with amplitudes above a threshold value of 0.7 are included. This threshold value is the standard deviation of the running mean JJAS MJO amplitude. Only the days closest to the center of the category are used, ensuring that all days included within each category are independent; these days have been circled in Fig. 5. These days are used to create an average anomaly map for each of the eight categories. Based on a nominal MJO period of 48 days, a cycle of 48 days is computed with each category representing a nominal 6-day average (Fig. 6).

Categories 5, 6, 7, 8, 1, 2, 3, and 4 correspond to the 6-day periods centered on day −24, −18, −12, −6, 0, 6, 12, and 18 of the cycle, respectively. The category and day numbers are shown in Fig. 6. Day 0 (category 1) corresponds to a phase of $\alpha = 0°$. The OLR anomaly map on day 0 (Fig. 6e) has a similar pattern to EOF1 (Fig. 4a). However, there are differences, as only the days within JJAS are included. Day 12 (category 3, $\alpha = 90°$), 24 and −24 (category 5, $\alpha = 180°$), and −12 (category 7, $\alpha = 270°$) are similar to EOF2, −EOF1, and −EOF2, respectively.

The OLR composites (Fig. 6) show large convective anomalies over the warm pool region. On day −24 (Fig. 6a) there is a large region of positive OLR anomalies (reduced convection) over the Indian Ocean with an area of negative OLR anomalies (enhanced convection) to the northeast. The positive OLR anomalies propagate northeastward to the western and central Pacific over the next 24 days. On day −12 (Fig. 6c) the positive OLR anomalies have moved eastward, covering Indonesia. A small region of negative OLR anomalies at 60°E is the start of the next active MJO in the western Indian Ocean. Six days later (day −6, Fig. 6d) these negative OLR anomalies have developed and continue to expand and intensify so that by day 0 (Fig. 6e) there is a large region of negative OLR anomalies over the Indian Ocean and a region of positive OLR anomalies to the northeast, that is, the opposite of the anomalies on day −24 (Fig. 6a). The OLR composites also show convective anomalies occurring over West Africa. On day −12 (Fig. 6c) there are negative OLR anomalies (enhanced convection) over the West African region, and on day 12 (Fig. 6g) there are some positive OLR anomalies that do not extend as far west. In both cases, OLR anomalies of the same sign occur over Central and South America at the same time and a few days previously.

The pattern of eastward-propagating convective anomalies over the equatorial warm pool, followed by anomalies of the opposite sign, describe the MJO (e.g., Madden and Julian 1994; Hendon and Salby 1994). The pattern of
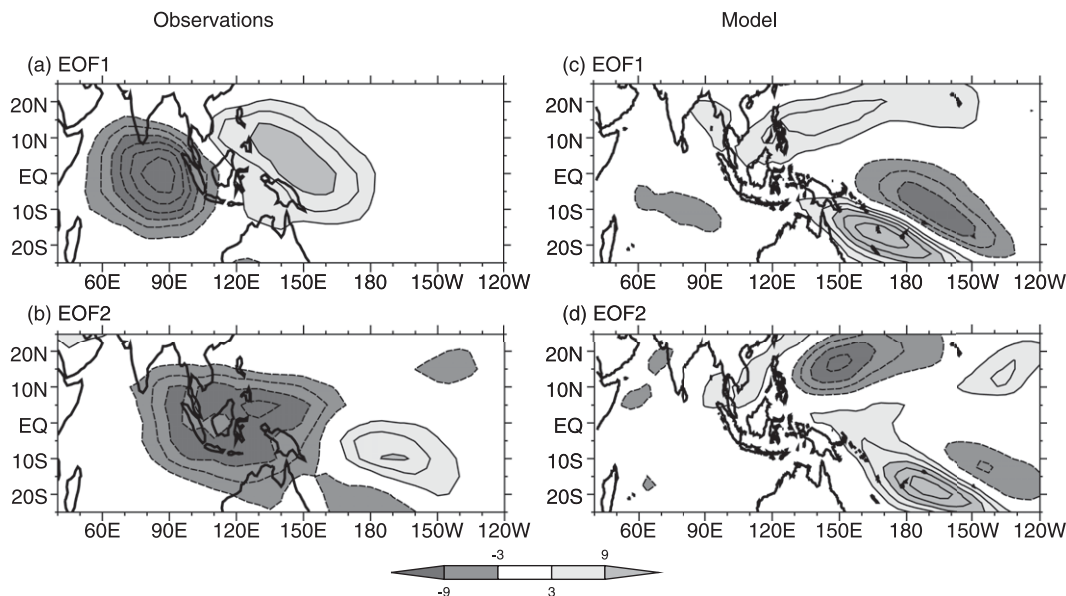
FIG. 4. EOF analysis of 10–200-day filtered OLR over the tropics (25°S–25°N) between 40° and 120°W from 1983 to 2004: (a) EOF1 and (b) EOF2 from satellite data: (c) EOF1 and (d) EOF2 from modeled data. Contour interval is 3 W m^{-2}. The zero contour is omitted and negative contours are dashed; shading is shown by the legend.

positive (negative) OLR anomalies over the warm pool occurring approximately 18 days before negative (positive) OLR anomalies over West Africa can also be seen in Fig. 6. This cycle of composites was produced based on an EOF analysis over the warm pool only. Hence, a robust link between the MJO and the WAM has been found, independently of whether the analysis is based on the WAM or the MJO. However, cause and effect cannot be unambiguously determined through purely observational studies. A carefully designed model experiment is now performed to test the hypothesis that the intraseasonal variability of the WAM arises as a forced response to the MJO.

4. Simulating the MJO forcing in a GCM

a. The Unified Model

The Met Office Unified Model (UM) is a GCM designed to run as a global, regional, or mesoscale model for forecasting and climate simulations. Version 4.5 uses a hydrostatic set of dynamical equations on a vertical hybrid sigma/pressure coordinate system and a regular latitude–longitude grid in the horizontal (Cullen 1993). The Unified Model has been shown to be one of the better GCMs at simulating tropical intraseasonal variability (Slingo et al. 1996).

The atmosphere-only model, version 4.5 [the Third Hadley Centre Atmosphere Model (HadAM3)], is run here linked to the Met Office Surface Exchange Scheme

(MOSES) 2.2. This version of the land surface scheme includes a tiled representation of the land surface. Surface fluxes and temperature are calculated for each surface type in a grid box and totaled depending on
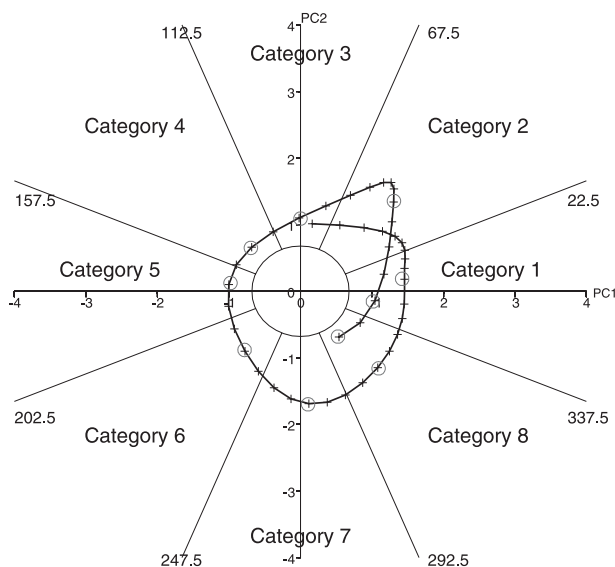

FIG. 5. Example amplitude and phase plot for 1 Jun to 13 Jul 1996, showing the anticlockwise rotation in phase space. The MJO has been divided up into eight categories depending on its phase and amplitude. The central circle, with an amplitude of 0.7, defines the region of no MJO activity. The circled dates are those closest to the middle of the category and are included in the anomaly maps.
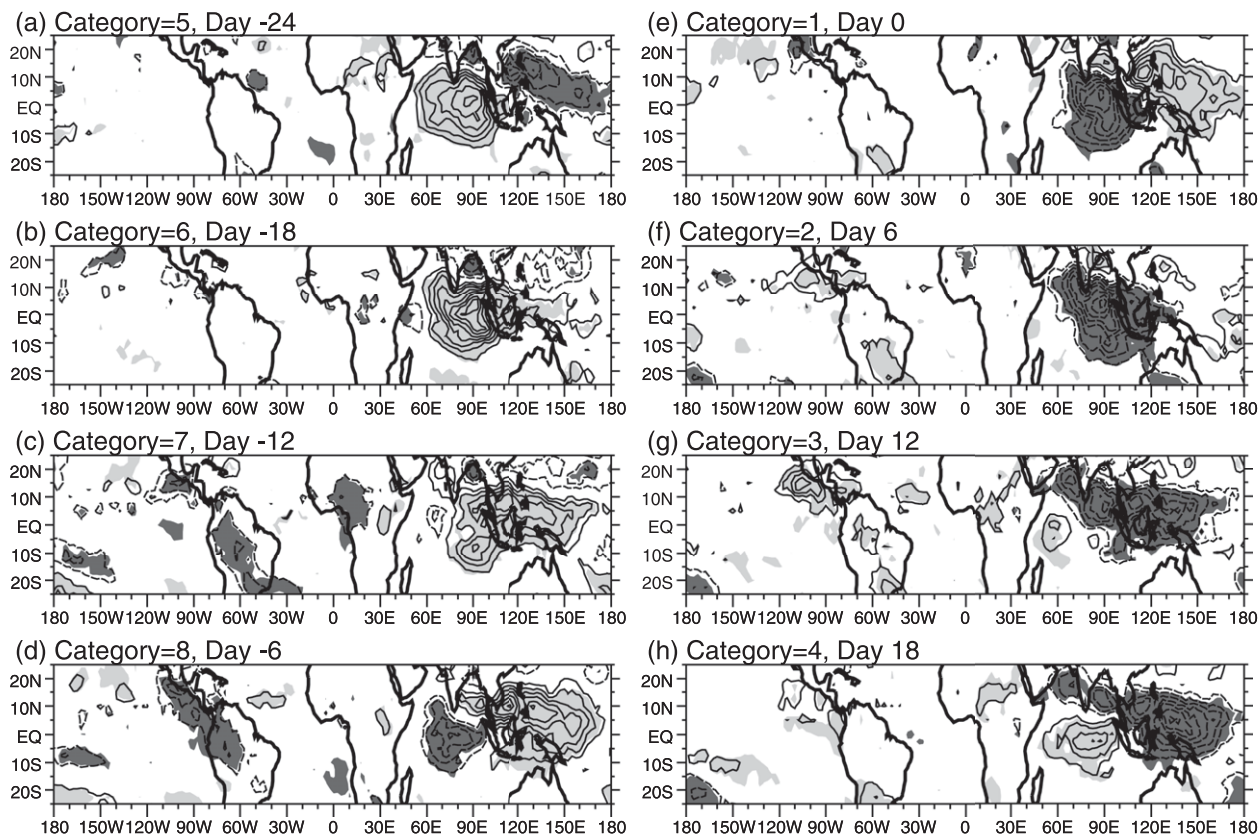
FIG. 6. Composite cycle of observed satellite OLR anomalies based on PC1 and PC2 from the warm pool analysis, June–September from 1983 to 2004 on days −24 to 18 of the 48-day MJO cycle: contour interval is 4 W m^{-2}, negative contours are dashed, and the zero contour is omitted. Shading indicates areas significant at the 95% level.

their fractional coverage. The model was run using the Gregorian calendar and 30 vertical levels, corresponding to a layer thickness of approximately 50 hPa in the midtroposphere. The use of 30 levels has been shown to improve the representation of the tropical intraseasonal variability (Inness et al. 2001) compared with the standard 19 levels. The albedo values over the Sahel are known to be underestimated in the original UM setup (Allan et al. 2005). These values have been replaced by more realistic values based on comparisons with satellite data. Dry, light soils now have a set albedo of 0.4.

A number of the soil-dependent hydraulic parameters [volumetric soil moisture content (SMC) at wilting point, volumetric SMC at critical point, saturated soil conductivity, and saturated soil water suction] have been altered owing to a misinterpretation when producing the original hydraulic parameters from sand, silt, and clay fractions in MOSES2. Osborne et al. (2004) found that changing these soil parameters had little effect on the precipitation. However, they do have a significant impact on soil moisture. Changing the soil hydraulic parameters results in more realistic values of

the field soil moisture capacity and bare soil evaporation over the region.

b. Modeled MJO link with West Africa

The West African–based EOF analysis was repeated using the modeled data to analyze the link between the WAM and the MJO in the model. The first EOF showed a similar pattern to that seen in the satellite data (Fig. 1), although the model produces larger anomalies. The model eigenvectors accounted for a lower percentage of the variance than the observations with the first eigenvector accounting for 12.1% of the variance. This was found to be well separated from the second (9.4%) and these were uncorrelated at the 95% level. Time-lagged composites were produced based on when PC1 of the modeled analysis is a maximum and above a threshold of one standard deviation. On day 0 (Fig. 7c) the enhanced convection over West Africa has a similar pattern as day 0 in the satellite analysis (Fig. 2c). On day −10 (Fig. 7b), there is suppressed convection over the warm pool along 15°N at 90° and 150°E; this is occurring farther north than in the satellite analysis (Fig. 2b). In
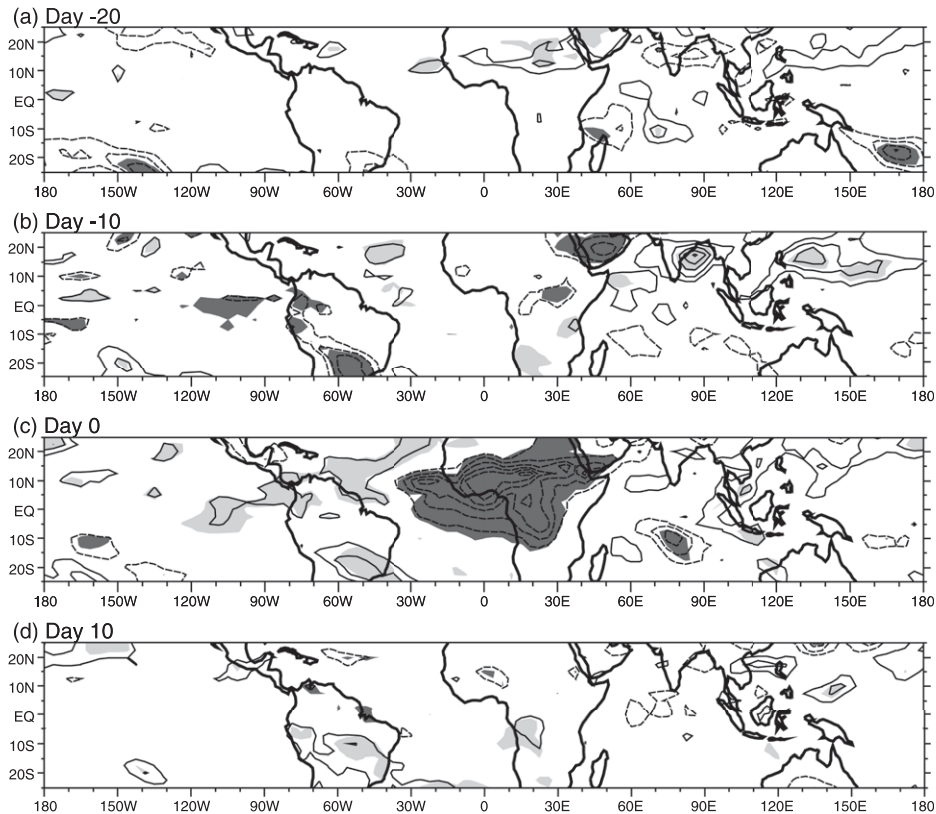
FIG. 7. Lagged composite maps of modeled OLR anomalies based on PC1 of 10–200-day filtered OLR over West Africa, June–September from 1983 to 2005 on days (a) −20, (b) −10, (c) 0, and (d) 10: contour interval is 3 W m^{-2}, negative contours are dashed, and the zero contour is omitted. Shading indicates the values significant at the 95% level.

the satellite composites there was a clear northeastward propagation of convective anomalies over the warm pool from day −20 to day 10; this does not occur in the modeled composites. This may be due to the representation of the MJO by the model.

The MJO in the model was analyzed using an EOF analysis performed over the warm pool region (25°S–25°N, 40°–120°W) on the 10–200-day filtered intraseasonal modeled OLR anomalies over the full years from 1983 to 2004. The first eigenvector accounted for 3.8% of the variance and was well separated from the next eigenvector, accounting for 3.4% of the variance, according to the criteria of North et al. (1982). This in turn was well separated from the following eigenvectors, which formed a degenerate set. The first two eigenvectors show the dominant mode of intraseasonal variability in the model (Figs. 4c,d). They do not represent the MJO. The model also avoids producing convective anomalies over the equator, where the majority of convective anomalies occurred in the satellite analysis. Producing a composite cycle of OLR anomalies based on these EOFs showed no eastward propagation.

c. Boundary conditions

The intrinsic MJO is poorly represented in the atmosphere-only version of the UM used here, as found above and in previous studies (e.g., Matthews et al. 1999; Inness et al. 2001). To examine the response over West Africa to the MJO, a realistic MJO needs to be simulated in the model. However, the main requirement for the experiment here is to force the equatorial Kelvin and Rossby waves over the warm pool; that is, a realistic latent heating anomaly is needed. This can be imposed cleanly by changing the model boundary conditions, specifically SSTs. SSTs are an important component of the MJO and tend to lead convection by 10–12 days (e.g., Shinoda et al. 1998; Woolnough et al. 2000; Maloney and Kiehl 2002). Applying a positive (negative) SST anomaly destabilizes (stabilizes) the atmosphere, leading to enhanced (suppressed) convection, positive (negative) latent heating anomalies, and upward (downward) motion. MJO atmospheric circulations can be forced as a response to intraseasonal tropical SST anomalies (Woolnough et al. 2001; Matthews 2004b; Klingaman
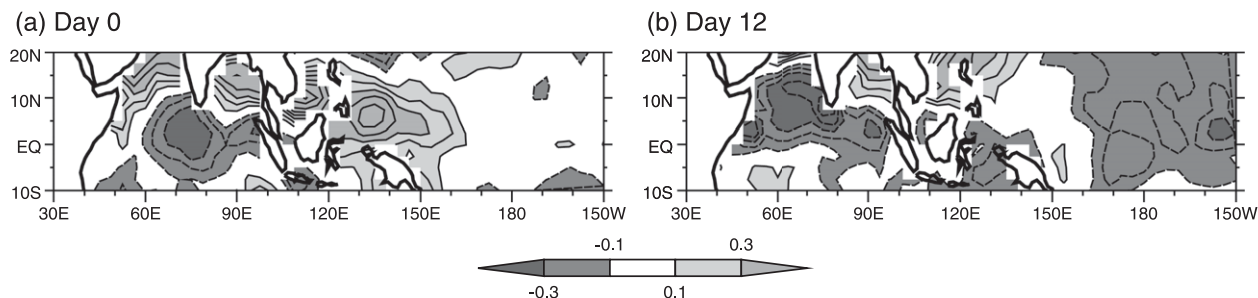
FIG. 8. SST anomalies used to force the model on (a) day 0 and (b) day 12 of the 48-day cycle: contour interval is 0.1 K, the zero contour is omitted, and negative contours dashed; shading is shown by the legend.

et al. 2008). The controversial issue of whether the MJO is fundamentally a coupled ocean–atmosphere phenomenon is not important here. The SST forcing is used here as a MJO generator, merely a means to the end of producing a realistic far-field response to what is possibly an artificially forced MJO.

First, the UM was run for 23 years as a control run forced by 90-day low-pass filtered daily SSTs from the NOAA OIv2 dataset. These SSTs will still contain interannual variability but will not have any coherent forcing on the intraseasonal scale, that is, from the MJO.

Second, a perturbation UM experiment was run, forced by observed MJO SST anomalies, as follows. A 48-day cycle of observed 10–200-day filtered intraseasonal anomalies of SST were produced based on the PC1 and PC2 time series of OLR, using the composite method described in section 3. The eight SST anomaly maps (one for each category) were linearly interpolated in time (each map is separated in time by 6 days from the next) to give a daily anomaly cycle of 48 days. The SST composites showed the strongest variability, and that which is likely to be associated with the MJO, occurring mainly between the east coast of Africa and the mid-Pacific. Hence, only the anomalies from 10°S to 20°N, 30°E to 150°W are used to force the model (Fig. 8).

Previous studies have found SST anomalies associated with the MJO are typically 0.25°–0.5°C (e.g., Shinoda et al. 1998; Maloney and Kiehl 2002). The SST anomalies found in our study ranged between 0.025° and 0.15°C. These smaller values are mainly a result of only using dates during June–September and the compositing technique. Also, the NOAA OIv2 SST data used here give an underestimate of the true strength of MJO SST anomalies (Klingaman et al. 2008). In this experiment, the SST anomalies are only used to create an MJO forcing in the model. In reality, the MJO is only partially coupled to the ocean and is not expected to be perfectly reproducible as a response to imposed SST anomalies (Matthews 2004b). Hence, to increase the SST anomalies to values of the order found previously

in observations and to increase the signal-to-noise ratio and successfully generate an atmospheric MJO, the values of the SST anomalies were increased by a factor of 4 (Fig. 8). These anomalies were added to the 90-day low-pass daily interpolated SST data used in the control run as a repeating 48-day anomaly cycle. The perturbation experiment was run as in the control run with the only difference being the SST boundary conditions.

The difference between the output from the perturbed run and the control run was taken for several variables and filtered using a 10–200-day Lanczos filter to remove variability outside this range. The repeating 48-day cyclic SST forcing was assumed to force a 48-day cyclic response in the model. This response was diagnosed by averaging over the 48-day cycles in the model, just using 10–200-day filtered data from the 122-day June–September seasons. The model was run for 23 years; hence each day in the model response cycle was an average of $23 \times 122/48 = 58$ independent days of data. The statistical significance of the values was found using a t test (Wilks 1995) with 58 degrees of freedom.

5. Modeled response to the imposed MJO SST anomalies

a. Convective response

The convective response of the model to the imposed MJO SST cycle can be seen from composite maps of OLR anomalies. Significant OLR anomalies occur over the whole tropics including parts of Africa (Fig. 9). On day -24, the SST anomalies imposed were of opposite sign to those shown in Fig. 8a. There is a region of positive OLR anomalies (reduced convection) over Indonesia, extending over India and the northern Indian Ocean (Fig. 9a) in response to the negative SST anomalies over the same region. Over the near-equatorial Indian Ocean at 70°E the positive SST anomalies have forced enhanced convective activity (negative OLR anomalies). The positive OLR anomalies have propagated slightly northward
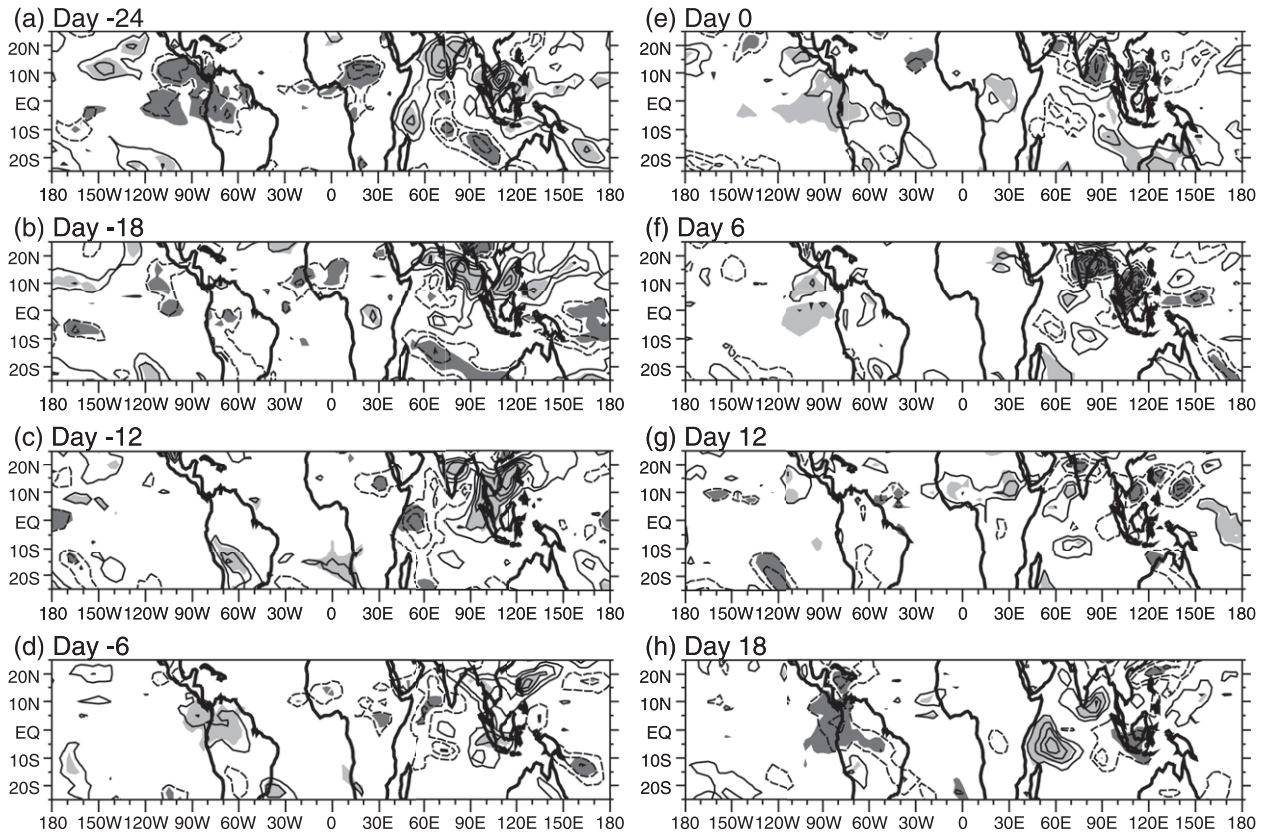
FIG. 9. Lagged composite maps of modeled OLR anomalies on days −24 to 18: contour interval is 4 W m^{-2}, the zero contour is omitted, and negative contours are dashed; shading indicates values significant at the 95% level.

and eastward by day −18 (Fig. 9b). On day −12 (Fig. 9c) the positive OLR anomalies have decreased both spatially and in magnitude and by day −6 (Fig. 9d) there are only small positive OLR anomalies present. On day 0 (Fig. 9e) the OLR anomalies over the warm pool have a similar pattern as on day −24 but of opposite sign, with negative OLR anomalies (enhanced convection) over the warm pool. The enhanced convection has then intensified by day 6 (Fig. 9f) and by day 12 (Fig. 9g) has propagated eastward and decreased in magnitude.

The modeled convective anomalies (Fig. 9) do not show as clear an eastward propagation of convective anomalies associated with the MJO as seen in the observations (Fig. 6). There appears to be a time lag between the modeled and observed anomalies with the modeled anomalies on day 0 (Fig. 9e) having a similar pattern to the observations on day 12 (Fig. 6g). In the model the OLR anomalies follow the SSTs much more closely in time than we would expect from the observations, with negative (positive) OLR anomalies forced by positive (negative) SST anomalies 4 days previously. This response was found by Fu and Wang (2004) and Matthews (2004b) who found that in atmosphere-only

models OLR tends to lag the SST anomalies by only 4 days compared to 12 days in the observations. The spatial area of the anomalies is smaller in the model. However, after accounting for the differences in timing, there are similarities between observational composites and the model response. The imposed warm pool MJO SST anomalies have succeeded in locally forcing MJO-like convective anomalies.

The model has also succeeded in producing a remote convective response outside the warm-pool forcing region. Given the experimental setup, we can now state unambiguously that these anomalies do arise as a remote response to the MJO forcing. Negative OLR anomalies occur over Central and South America on days 18 and −24 in the model and positive OLR anomalies on day −6 to day 6 (Fig. 9). Convective anomalies of the same sign occur over West Africa a few days later. The enhanced convection (negative OLR anomalies) first occurs mainly over the central Sahel on day −24 and farther west, over the western Sahel, on day −18. Suppressed convection (positive OLR anomalies) occurs over central Africa on day 0 (Fig. 9e) and over West Africa on day 12 (Fig. 9g). This westward-propagating

signal in convective anomalies has also been found in observational data (Janicot et al. 2009).

b. Equatorial waves

The hypothesis that dry equatorial Kelvin and Rossby waves are responsible for transmitting the warm-pool convective signal to Africa is examined here, using a zonal cross section along the equator of the temperature and zonal and vertical wind anomalies throughout the troposphere (Fig. 10). From day 0 to day 6, negative SST anomalies lead to a region of suppressed convection between 70° and 110°E (Figs. 9e,f). There are associated latent heating anomalies in the midtroposphere resulting in negative temperature anomalies at 500 hPa at these longitudes (Fig. 10f). There is ascent to the east and descent coincident with these negative temperature anomalies, with low-level westerly and upper-level easterly wind anomalies completing the circulation. Six days later (day 12) the positive OLR anomalies over the warm pool are still present (Fig. 9g) and the negative temperature anomalies (Fig. 10g) have deepened, extending from the surface (1000 hPa) to 300 hPa. By day 18, the suppressed convection over the warm pool has intensified, and the response to this is shown in the negative temperature signal throughout the troposphere (Fig. 10h) that has extended eastward across the Pacific. There is ascent ahead of these negative temperature anomalies at 80°W, which leads to adiabatic cooling. The resulting negative temperature anomalies over the Pacific (Fig. 10h) extend from the surface (1000 hPa) up to the tropopause (150 hPa). This is consistent with a dry Kelvin wave being forced by the negative latent heating anomalies. The wave propagates eastward, leaving a cold temperature signal in its wake with ascent ahead of the wave.

The negative temperature anomalies act to destabilize the whole column, leading to enhanced convection over the eastern Pacific and Central America (Figs. 9h,a). This enhanced convection then leads to positive midtropospheric latent heating and weak positive temperature anomalies at 600 hPa, 100°W (Figs. 10a,b). However, the main negative temperature anomalies associated with the cold Kelvin wave continue to move eastward.

On day 24/−24 (Fig. 10a) the deep negative temperature anomalies extend throughout the troposphere across the majority of the tropics. Over West Africa (0° longitude) the deep negative temperature anomalies lead to destabilization of the entire troposphere, enhancing convection over the region (Fig. 9a). To the west of West Africa there are upper-level easterly and low-level westerly anomalies, consistent with a remote Kelvin wave response to the suppressed convection at 120°E. These low-level westerlies may increase the boundary layer moisture supply to the region, resulting in enhanced convection. There is ascent and latent heating over West Africa that further intensifies in response to the enhanced convection.

Day −24 is also the start of the opposite phase of the MJO signal with positive SST anomalies leading to enhanced convection over the warm pool. This results in positive latent heating anomalies and a region of positive temperature anomalies between 60° and 110°E (600–200 hPa, Fig. 10a). There is descent to the east and ascent coincident with these positive temperature anomalies. On day −18 (Fig. 10b) the negative temperature anomalies exist in the upper troposphere over the whole tropics with positive temperature anomalies in the lower troposphere between 30° and 90°E forced by the positive SST anomalies. The positive temperature anomalies have extended throughout the troposphere and propagated eastward by day −12 (Fig. 10c) with downward motion ahead of the positive temperature anomalies. This is consistent with the propagation of a Kelvin wave with descent at the wave front (90°W). The deep descent leads to adiabatic warming and positive temperature anomalies throughout, from the surface to the tropopause. The positive temperature anomalies act to stabilize the whole troposphere, resulting in suppressed convection over the eastern Pacific and Central America on day −6 (Fig. 9d). By day 0 (Fig. 10e) the positive temperature anomalies and associated descent and upper-level westerlies and low-level easterlies have propagated eastward throughout the troposphere, reaching Africa. The descent at 20°E leads to adiabatic warming and suppressed convection there (Fig. 9e). The structure of the temperature and winds is consistent with an equatorial Kelvin wave being forced by the positive latent heating anomalies associated with positive SST anomalies and positive midtropospheric temperature anomalies stabilizing the atmosphere. The anomalous upper-level easterlies and low-level westerlies between 30° and 150°E are consistent with an equatorial Rossby wave structure, discussed in detail later.

This eastward and westward propagation of the equatorial waves and the associated temperature and zonal wind anomalies can be shown more clearly using composite Hovmöller diagrams, averaged over the equator, between 10°S and 10°N. A Hovmöller diagram of equatorial temperature anomalies at 300 hPa (Fig. 11) and OLR anomalies (averaged between 5°N and 15°N) shows positive and negative temperature anomalies propagating from between 90° and 180°E, both eastward and westward to approximately 0° longitude 10 days later (highlighted by thick solid lines). For example, on day −26 (in the previous cycle) negative SST anomalies result in the occurrence of negative midtropospheric
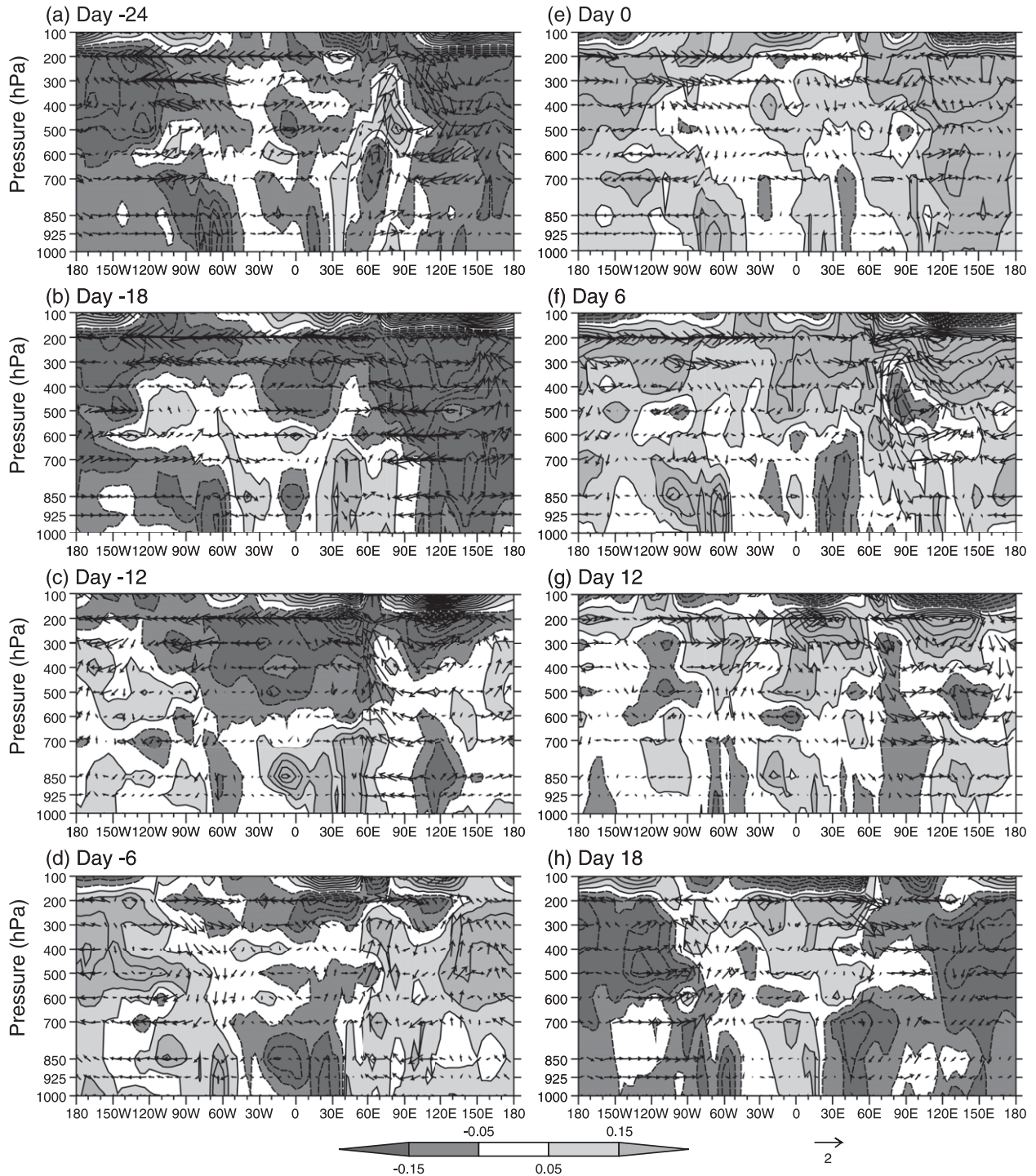
FIG. 10. Longitude–pressure cross section composites of modeled temperature, zonal wind (u), and vertical velocity (ω) anomalies averaged between 10°S and 10°N on days −24 to 18: temperature contour interval is 0.1 K, negative contours are dashed; first positive contour is at 0.05 K. Shading is shown by the legend. Zonal and vertical wind is plotted as a pseudovector with a reference vector of 2 m s^{-1} for u and 0.02 Pa s^{-1} for ω.
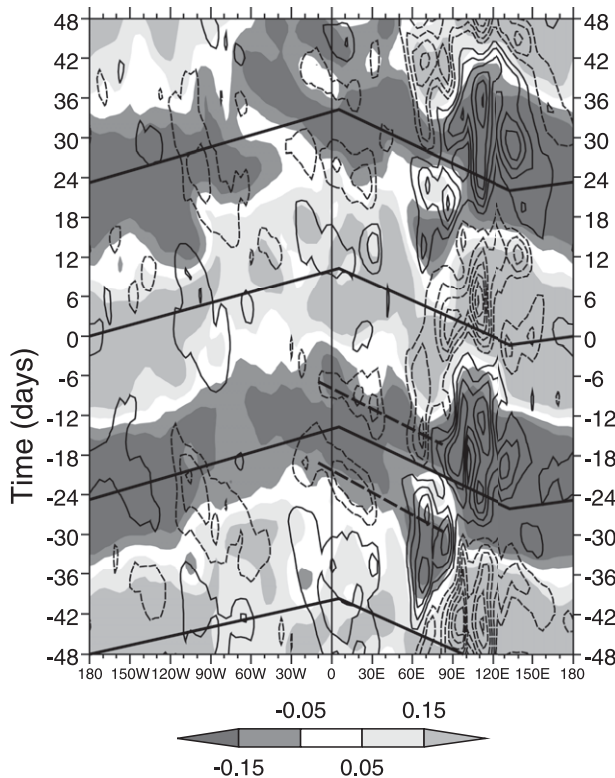
FIG. 11. Composite Hovmöller diagram of two cycles (from day −48 to 48) of modeled temperature anomalies at 300 hPa (shading) averaged between 10°S and 10°N and OLR anomalies (contours) averaged between 5° and 15°N: OLR contour interval is 0.3 W m^{-2}, negative contours are dashed, and the zero contour is omitted. Shading is shown by the legend. The thick solid lines indicate the propagation of the peak temperature anomalies. The thick dashed lines indicate the propagation of the two individual equatorial Rossby waves within the envelope of negative temperature anomalies.

temperature anomalies over the warm pool, east of 90°E (Fig. 11). These negative midtropospheric temperature anomalies then propagate both eastward and westward, meeting at around 0° longitude on day −15. This is consistent with the negative latent heating anomalies forcing an eastward-propagating dry Kelvin wave and a westward-propagating Rossby wave. The speed of propagation is similar to that calculated from observations in section 3, with the Kelvin wave propagating at approximately 32 m s^{-1} and the Rossby wave at 17 m s^{-1}. In the observations (Fig. 3), the OLR anomalies over West Africa were coincident with the peak in temperature anomalies. However, in the modeled results there are two peaks in the enhanced convection. The first is on day −24 when the temperature forcing first arrives, and the second is on day −9.

These OLR anomalies propagate westward themselves, along with the westward propagating envelope of

negative temperature anomalies associated with the equatorial Rossby wave. Hence, it appears that the westward-propagating dry Rossby wave has the largest influence on convection (the Rossby wave structures are discussed later). The westward propagating waves are indicated by the thick dashed lines. For example, between 60° and 90°E on day −30 there are positive OLR anomalies and associated negative midtropospheric temperature anomalies. The temperature anomaly then propagates westward as a forced (dry) equatorial Rossby wave. By day −26 this has resulted in enhanced convection at 30°E. The troposphere is continuously destabilized as the negative temperature anomalies associated with the dry Rossby waves propagate westward, resulting in the westward propagation of OLR anomalies over West Africa. A second maximum in enhanced convection on day −9 results from temperature and OLR anomalies between 90° and 120°E on day −18. The importance of the Rossby wave and the resulting westward propagation of the West African convection is consistent with the findings of Janicot et al. (2009). However, Janicot et al. found that it was convectively coupled Rossby waves originating from the Indian monsoon region, which propagate at approximately 5 m s^{-1} (Wheeler et al. 2000). Here, the westward-propagating OLR anomalies have the same phase speed as the forcing temperature anomalies (17 m s^{-1}). Ultimately the occurrence of convective anomalies will force a temperature response that may lead to the Rossby wave becoming convectively coupled. This cannot be determined from the results presented here.

Janicot et al. (2009) found the dry and convectively coupled Kelvin waves to have little influence on West African convection. In this study the convective signal over the Americas (120°–90°W) is consistent with forcing by the dry Kelvin wave due to deep ascent and adiabatic cooling resulting in negative temperature anomalies (from the surface to the tropopause) and destabilization of the whole troposphere.

In the opposite half of the cycle, peak positive midtropospheric temperature anomalies occur over the warm pool east of 120°E on day 2 and propagate eastward and westward around the globe, reaching Africa on day 9 (Fig. 11). The positive midtropospheric temperature anomalies will act to stabilize the atmosphere, resulting in suppressed convection as seen over West Africa on day 12 (Figs. 11 and 9g). There is only one maximum in suppressed convection whose timing is consistent with the meeting of the peak temperature signal. Positive temperature anomalies first occur over the African region on day 0, accounting for the suppressed convection over central Africa (Fig. 9e).
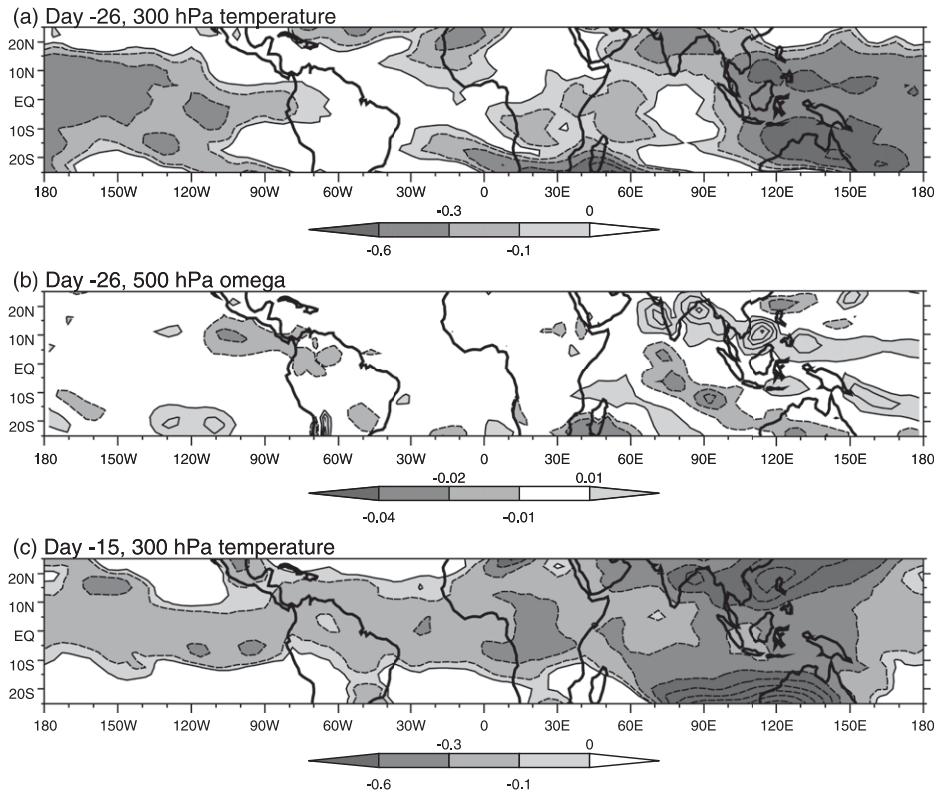
FIG. 12. Lagged composite maps of modeled 300-hPa temperature anomalies on (a) day −26 (in the previous cycle) and (c) day −15, contours plotted at 0, −0.1, −0.3, then every −0.3 K. (b) Modeled vertical velocity at 500 hPa on day −26: contours plotted every 0.01 Pa s⁻¹, the first contours at ±0.01 Pa s⁻¹. Negative contours are dashed; shading is shown by the legend.

In general, the westward propagation of the convective anomalies over West Africa from 30°E to 5°W is consistent with the findings of Janicot et al. (2009). This is different from the results of Maloney and Shaman (2008), who found the variability in precipitation to be almost stationary, likely due to their different methodology.

The dry equatorial Kelvin and Rossby wave structures can be seen more clearly in the maps of 300-hPa temperature anomalies and 500-hPa vertical velocity anomalies (Fig. 12). On day −26 (in the previous cycle) there is a negative temperature anomaly over the warm pool, where there is reduced convection (e.g., day −24, Fig. 9a). The Kelvin wave can be seen as a tongue of negative temperature anomalies extending to the east along the equator. The off-equatorial minima in temperature anomalies between 120° and 150°E are consistent with an equatorial Rossby wave structure. The vertical velocity map (Fig. 12b) indicates ascent (negative vertical velocity) at the Kelvin wave front between 110° and 60°W. There are two off-equatorial maxima in ascent associated with the Rossby wave at 80°E. On day

−15 when the minimum temperature anomalies occur over West Africa (Fig. 11), there are negative temperature anomalies over the entire tropics (Fig. 12c). The Kelvin wave has propagated eastward and the Rossby wave westward, completing a circuit of the equator. The modeled Kelvin and Rossby wave structures and their propagation are consistent with those when the analysis is based on observations of the maximum in convection over West Africa (Fig. 6 in Matthews 2004a).

As well as temperature anomalies, equatorial Kelvin and Rossby waves have associated anomalous upper- and lower-tropospheric equatorial zonal wind anomalies (Fig. 13). The thick lines in Fig. 13 highlight the propagation of the temperature anomalies in Fig. 11. Between 150°E and 30°W the positive (negative) mid-tropospheric temperature anomalies (Fig. 11) have associated upper-level westerly (easterly) anomalies (Fig. 13a) and low-level easterly (westerly) anomalies (Fig. 13b). This is consistent with the propagation of an equatorial Kelvin wave (Gill 1980). The low-level zonal wind anomalies are not coherent between 30°W and 60°E (Fig. 13b). However, the anomalous upper-level
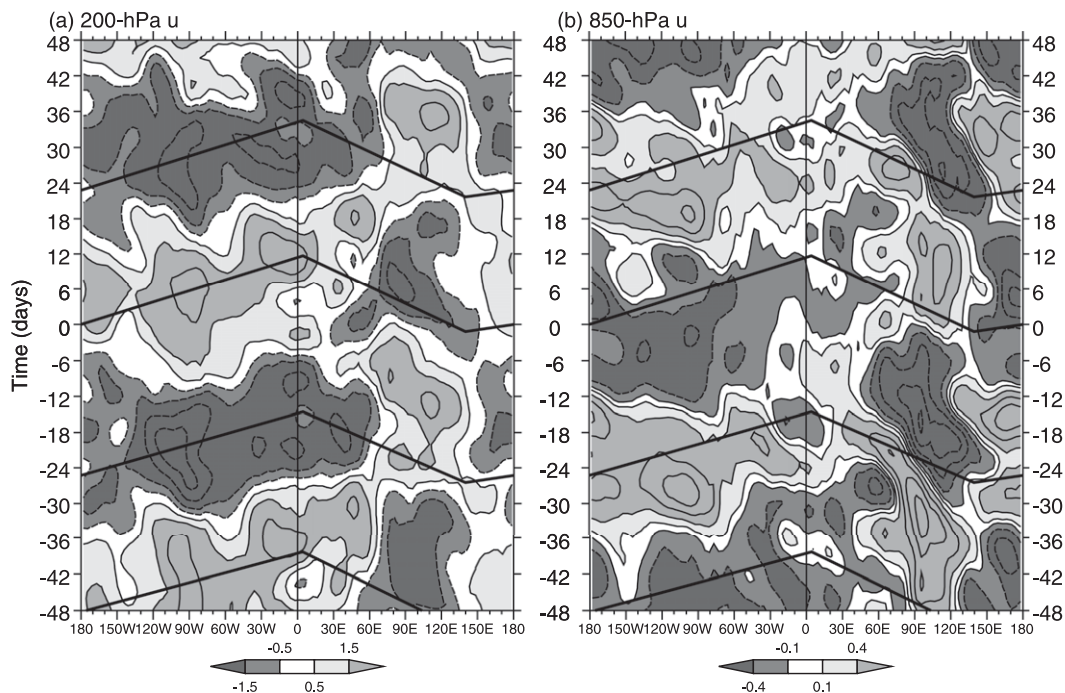
FIG. 13. Composite Hovmöller diagram of modeled zonal wind anomalies at (a) 200 and (b) 850 hPa averaged between 10°S and 10°N: contour interval is ±0.5, 1.5, then every 1 m s⁻¹ in (a) and ±0.1, 0.4, then every 0.4 m s⁻¹ in (b). Shading is shown by the legends. The thick lines indicate the propagation of the temperature anomalies in Fig. 11.

zonal winds continue to propagate eastward to approximately 60°E (Fig. 13a). Comparison between the Hovmöller diagrams show that the low-level zonal wind anomalies (Fig. 13b) propagate first, approximately 6 days before the temperature anomalies (Fig. 11) and 200-hPa zonal winds (Fig. 13a). Maloney and Shaman (2008) found the winds forced by the MJO propagated much slower than the temperature anomalies. This is not supported by the model results here where there are similar propagation speeds of both zonal wind anomalies and temperature anomalies.

The zonal winds along the equator associated with a theoretical Rossby wave are of opposite sign to those of the Kelvin wave. A slight westward propagation of the modeled zonal wind anomalies can be seen, for example, on day 0 at 150°E when there are positive midtropospheric temperature anomalies (Fig. 11); the anomalous zonal winds at 200 hPa are easterly. These propagate westward to approximately 60°E by day 6 (Fig. 13a). The 850-hPa winds are westerly from 90° to 120°E between day 0 and day 6 (Fig. 13b) before fading away. This highlights that it is equatorial Kelvin and Rossby waves that are forced by the SST anomalies and the resulting latent heating anomalies over the warm pool, propagating around the globe and meeting over West Africa. The associated midtropospheric tempera-

ture anomalies act to destabilize/stabilize the atmosphere, resulting in convective anomalies.

The results shown in this section support the first mechanism suggested by Matthews (2004a). Equatorial waves are forced by the negative latent heating anomalies associated with positive OLR anomalies and negative SST anomalies over the warm pool. The equatorial waves meet over West Africa where their associated negative temperature anomalies act to destabilize the atmosphere, resulting in enhanced convection over West Africa. The two other suggested mechanisms of enhanced boundary layer moisture supply and increased shear on the AEJ will now be tested.

c. Moisture supply

Matthews (2004a) based his analysis on the dominant mode of convection over West Africa. It was found that, when there was enhanced convection over West Africa, there was an increase in the southwesterly monsoon flow and a large area of positive specific humidity anomalies at 925 hPa (Fig. 9b in Matthews 2004a). It was suggested that the southwesterly flow increased the moisture supply to the region, creating conditions more favorable to convection. However, from this observational analysis it was not possible to distinguish whether the increased moisture supply caused the convective
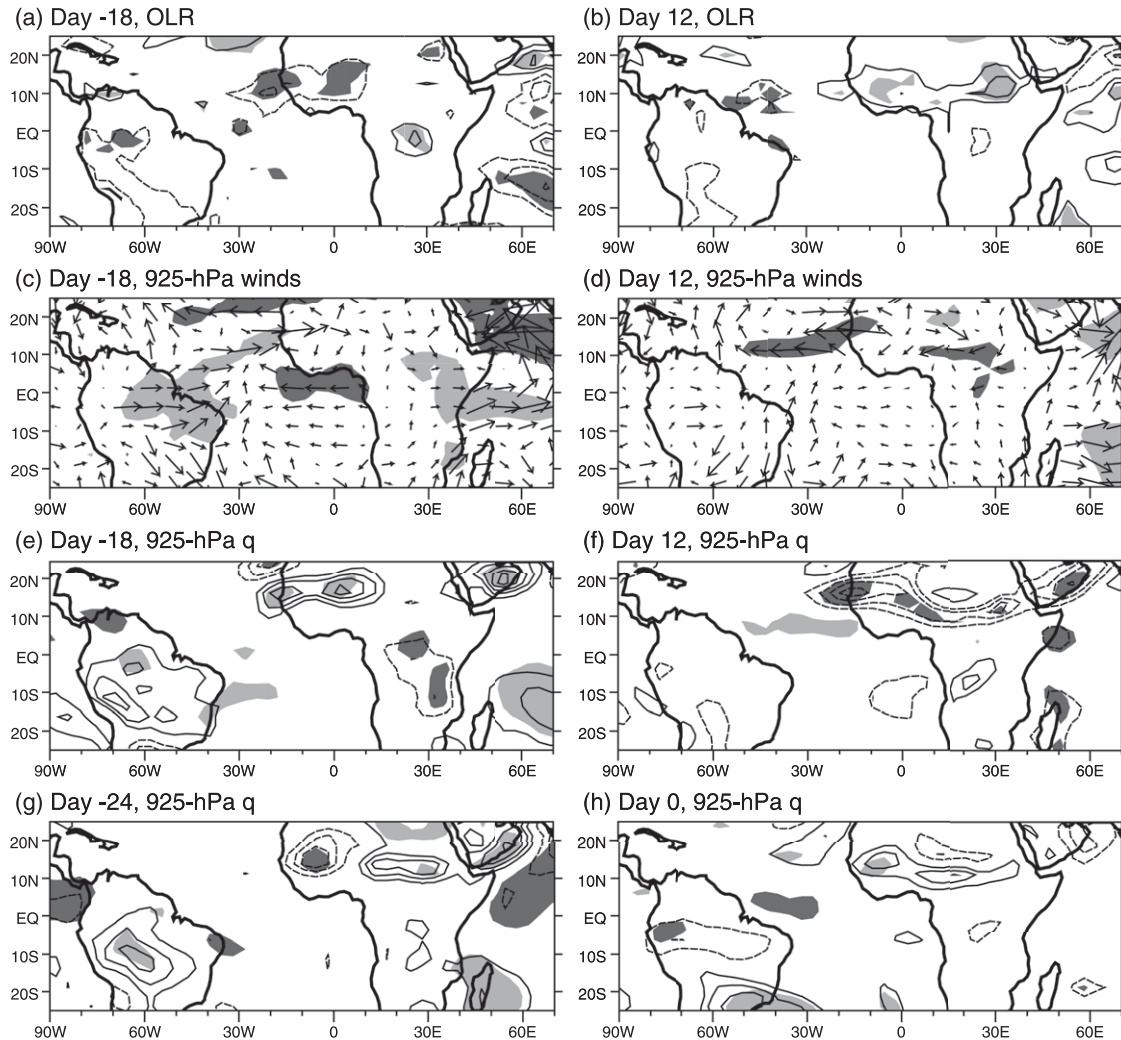
FIG. 14. Composite maps of modeled OLR anomalies on (a) day −18 and (b) day 12, contour interval is 4 W m^{-2}; 925-hPa wind vector anomalies on (c) day −18 and (d) day 12, only alternate vectors plotted. Anomalous specific humidity at 925 hPa on (e) day −18, (f) day 12, (g) day −24, and (h) day 0, contour interval is 0.2 g kg^{-1}. Shading indicates the anomalies significant at the 95% significance level [just the zonal wind component for (c) and (d)].

anomalies over West Africa or the moisture anomalies occurred as a result of the convection.

　　The analysis in this modeling study is based on imposed SST anomalies and the forced convective anomalies over the warm pool. Figure 10a shows low-level westerly anomalies, associated with an equatorial Kelvin wave, to the west of West Africa on day −24 when there is enhanced convection over the region (Fig. 9a). Figure 14 shows the OLR anomalies on days −18 (enhanced convection over West Africa) and day 12 (reduced convection over West Africa) and the corresponding wind and specific humidity anomalies at 925 hPa. On day −18 the wind anomalies at 925 hPa (Fig. 14c) are westerly over the Atlantic along 10°N and this may result in advection of more moisture into the African re-

gion. Along the equator there are significant easterly anomalies out of the central African region. There is a region of positive specific humidity anomalies present at 10°N (Fig. 14e) in the same area as the enhanced convection. However, the equatorial wave forcing (Fig. 11) and convective anomalies (Fig. 9a) first arrived over West Africa on day −24 when there are negative specific humidity anomalies at 15°N, 0° longitude (Fig. 14g). This is the region where convection develops on day −18 (Fig. 14a). This suggests that the mechanism of enhanced boundary layer moisture suggested by Matthews (2004a) is an effect of the enhanced convection rather than a mechanism causing it. Moisture convergence occurring as a result of the convective heating was also found by Maloney and Shaman (2008), who based their analysis
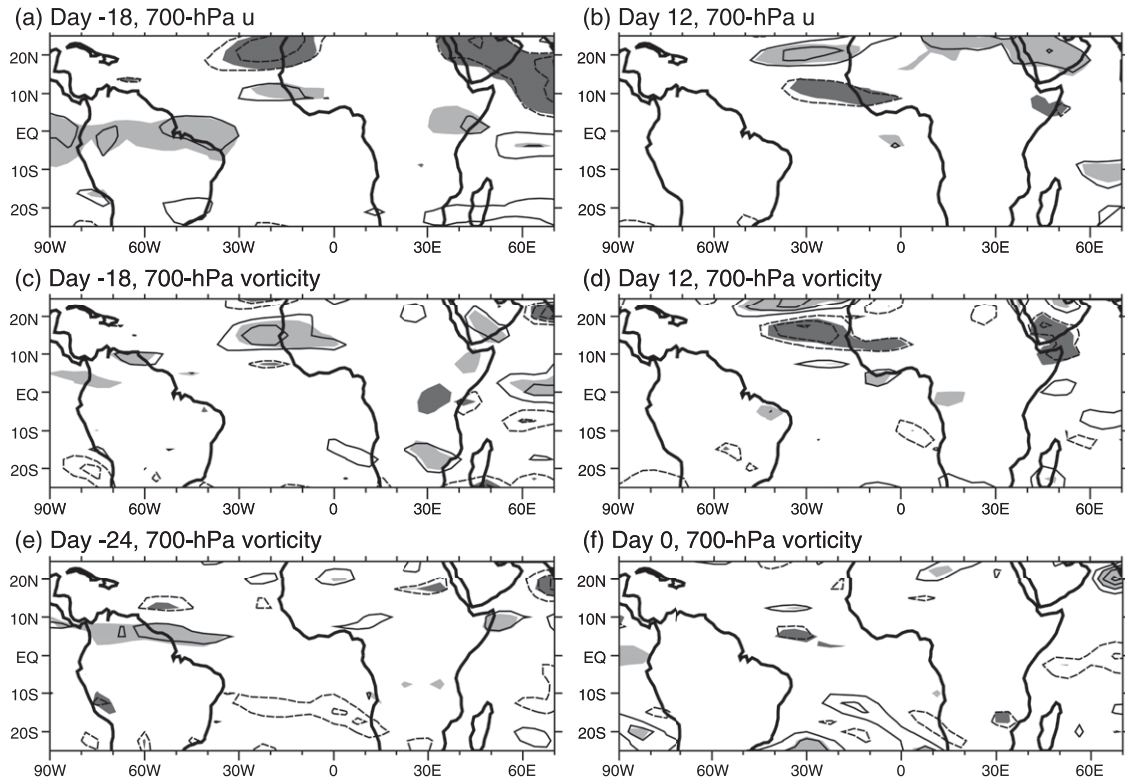
FIG. 15. Composite maps of modeled zonal wind anomalies at 700 hPa on (a) day −18 and (b) day 12, contour interval is 1 m s^{-1}. Anomalous vorticity anomalies at 700 hPa on (c) day −18, (d) day 12, (e) day −24, and (f) day 0, contour interval is 2×10^{-6} s^{-1}. Shading indicates anomalies significant at the 95% significance level.

on the intraseasonal variability of satellite precipitation data.

On day 12, when the positive midtropospheric temperature anomalies peak over West Africa (Fig. 11), there is a small region of reduced convection at 10°N (Fig. 14b). There are some easterly wind anomalies to the east of West Africa at 10°N (Fig. 14d). There is also a band of negative specific humidity anomalies at 10°N. However, on day 0 when the positive midtropospheric temperature anomalies (Fig. 11) and suppressed convection anomalies (Fig. 9e) first arrive over central Africa, there are positive specific humidity anomalies over the region where suppressed convection occurs over the following days.

These results imply that not only is the increased boundary layer moisture a result of the enhanced convection over the region but also, when the equatorial wave forcing first arrives there, conditions are unfavorable with decreased low-level moisture.

d. Barotropic instability of the African easterly jet

The third mechanism suggested was that enhanced horizontal shear on the African easterly jet (AEJ) causes the jet to become more barotropically unstable

and results in an increase in AEW activity. This increased AEW activity may then enhance the convective activity over West Africa. Matthews (2004a, Fig. 9d) showed a large area of enhanced vorticity at the latitude of the AEJ.

In the present study, the anomalous 700-hPa zonal winds on day −18 (Fig. 15a) show small regions of positive and negative anomalies off the West African coast at 10° and 20°N respectively and positive vorticity anomalies in between (Fig. 15c). These occur too far west to have an influence on convection over West Africa associated with AEW activity. On day −24 when the forcing first occurs, there are no vorticity anomalies (Fig. 15e). This suggests that the third mechanism, like the second, is likely a result of the enhanced convection over West Africa rather than a cause.

In the opposite half of the cycle (day 12), there is a similar spatial pattern of anomalies as day −18 but with opposite sign and negative vorticity anomalies off the coast of West Africa (Fig. 15d). Again, when the forcing waves first arrive, on day 0 (Fig. 15f), there are no significant anomalies over the region that convection occurs. As with the enhanced boundary layer moisture, the increased shear on the AEJ leading to enhanced

AEW activity appears to be a result of the convective anomalies rather than a controlling mechanism.

6. Conclusions

A link has been established between the intraseasonal variability over the warm pool, specifically the MJO, and convection over West Africa. A cycle of MJO SST anomalies were created based on the first two modes of observed intraseasonal variability over the warm pool. These SST anomalies were applied as boundary conditions in an atmospheric GCM and used to generate MJO convective and latent heating anomalies over the warm pool region. Composites of the differences between the control and perturbation runs showed significant anomalies in several variables over West Africa and the rest of the tropics. Hence, in the model simulation, convective anomalies in the West African monsoon were forced unambiguously by MJO-like convection over the warm pool.

This study supports work by Matthews (2004a), who based his observational analysis on the dominant mode of convection over West Africa and found that this appeared to arise, at least partly, as a remote response to convective anomalies over the warm pool. The proposed mechanism of equatorial waves being forced by latent heating anomalies over the warm pool is supported by the model results (section 5b). These dry equatorial Kelvin and Rossby waves propagate in opposite directions around the globe, meeting over West Africa where the associated negative temperature anomalies act to destabilize the troposphere, resulting in anomalous ascent and enhanced convection over Africa. Positive temperature anomalies stabilize the troposphere, resulting in descent and suppressed convection over West Africa. However, it is the Rossby wave that appears to have the main influence on convection over West Africa, and the convective anomalies propagate westward over West Africa. The findings of a westward-propagating convective signal over West Africa are consistent with the observational results of Janicot et al. (2009).

Convective anomalies over the eastern Pacific and Central America were also forced by the MJO in the model. The negative temperature anomalies associated with the cold Kelvin wave act to destabilize the atmosphere, resulting in enhanced convection. Positive temperature anomalies associated with descent and a warm Kelvin wave similarly result in suppressed convection over the eastern Pacific region, consistent with the observational results.

The propagation of dry equatorial waves is seen in the Hovmöller diagrams of upper- and lower-tropospheric zonal winds (Fig. 13) and midtropospheric temperature anomalies (Fig. 11). Associated with the Kelvin wave response are anomalous low-level zonal winds that act to increase (decrease) the monsoon flow. Matthews (2004a) found a significant increase in low-level specific humidity anomalies associated with the increased monsoon flow when enhanced convection occurred over West Africa. However, this observational study was unable to differentiate between cause and effect. This mechanism of moisture convergence was also found to be important by Janicot et al. (2009). The current model study suggests that increased low-level specific humidity and increased monsoon flow are a result of enhanced convection over West Africa rather than a cause. This result is consistent with the findings of Maloney and Shaman (2008) who based their analysis on the precipitation variability. Similarly, the increase in cyclonic shear on the AEJ leading to enhanced barotropic instability and enhanced AEW is also found to be a result of the convective activity over West Africa rather than a cause.

Even though the atmosphere-only model used in this study is known to be relatively poor at representing the MJO, the results suggest a robust link between the MJO and West Africa. This suggests that it may be possible to predict part of the variability in the WAM with a 15–20-day lead time, particularly given the recent success of operational statistical forecast models of the MJO (Wheeler and Hendon 2004; Love et al. 2008). As modeling capability continues to increase and with an improved representation of the MJO, this may also lead to better forecasting ability over West Africa.

REFERENCES

Allan, R. P., A. Slingo, S. F. Milton, and I. Culverwell, 2005: Exploitation of Geostationary Earth Radiation Budget data using simulations from a numerical weather prediction model: Methodology and data validation. *J. Geophys. Res.,* **110,** D14111, doi:10.1029/2004JD005698.

Annamalai, H., and J. M. Slingo, 2001: Active/break cycles: Diagnosis of the intraseasonal variability of the Asian summer monsoon. *Climate Dyn.,* **18,** 85–102.

Arkin, P. A., and P. E. Ardanuy, 1989: Estimating climatic-scale precipitation from space: A review. *J. Climate,* **2,** 1229–1238.

Cullen, M. J. P., 1993: The unified forecast/climate model. *Meteor. Mag.,* **122,** 81–94.

Diedhou, A., S. Janicot, A. Viltard, P. de Felice, and H. Laurent, 1999: Easterly wave regimes and associated convection over West Africa and tropical Atlantic: Results from the NCEP/ NCAR and ECMWF reanalyses. *Climate Dyn.,* **15,** 795–822.

Douville, H., 2002: Influence of soil moisture on the Asian and African monsoons. Part II: Interannual variability. *J. Climate,* **15,** 701–720.

Duchon, C. E., 1979: Lanczos filtering in one and two dimensions. *J. Appl. Meteor.,* **18,** 1016–1022.

Folland, C. K., T. N. Palmer, and D. E. Parker, 1986: Sahel rainfall and worldwide sea temperatures, 1901–85. *Nature,* **320,** 602–607.

Fu, X., and B. Wang, 2004: Differences of boreal summer intraseasonal oscillations simulated in an atmosphere–ocean coupled model and an atmosphere-only model. *J. Climate,* **17,** 1263–1270.

Gill, A. E., 1980: Some simple solutions for heat-induced tropical circulation. *Quart. J. Roy. Meteor. Soc.,* **106,** 447–462.

Grodsky, S. A., and J. A. Carton, 2001: Coupled land/atmosphere interactions in the West African monsoon. *Geophys. Res. Lett.,* **28,** 1503–1506.

Gu, G., R. F. Adler, G. J. Huffman, and S. Curtic, 2004: African easterly waves and their association with precipitation. *J. Geophys. Res.,* **109,** D04101, doi:10.1029/2003JD003967.

Hendon, H. H., and M. L. Salby, 1994: The life cycle of the Madden–Julian oscillation. *J. Atmos. Sci.,* **51,** 2225–2237.

Inness, P. M., J. M. Slingo, S. J. Woolnough, R. B. Neale, and V. D. Pope, 2001: Organization of tropical convection in a GCM with varying vertical resolution: Implications for the simulation of the Madden-Julian oscillation. *Climate Dyn.,* **17,** 777–793.

Janicot, S., and B. Sultan, 2001: Intra-seasonal modulation of convection in the West African monsoon. *Geophys. Res. Lett.,* **28,** 523–526.

——, A. Harzallah, B. Fontaine, and V. Moron, 1998: West African monsoon dynamics and eastern equatorial Atlantic and Pacific SST anomalies (1970–88). *J. Climate,* **11,** 1874–1882.

——, F. Mounier, N. M. J. Hall, S. Leroux, B. Sultan, and G. N. Kiladis, 2009: The dynamics of the West African monsoon. Part IV: Analysis of 25–90-day variability of convection and the role of the Indian monsoon. *J. Climate,* **22,** 1541–1565.

Klingaman, N. P., H. Weller, J. M. Slingo, and P. M. Inness, 2008: The intraseasonal variability of the Indian summer monsoon using TMI sea surface temperatures and ECMWF reanalysis. *J. Climate,* **21,** 2519–2539.

Lebel, T., F. Delclaux, L. Le Barbe, and J. Polcher, 2000: From GCM scales to hydrological scales: Rainfall variability in West Africa. *Stochastic Environ. Res. Risk Assess.,* **14,** 275–295.

Liebmann, B., and C. A. Smith, 1996: Description of a complete (interpolated) outgoing longwave radiation dataset. *Bull. Amer. Meteor. Soc.,* **77,** 1275–1277.

Love, B. S., A. J. Matthews, and G. J. Janacek, 2008: Real-time extraction of the Madden–Julian oscillation using empirical mode decomposition and statistical forecasting with a VARMA model. *J. Climate,* **21,** 5318–5335.

Madden, R. A., and P. R. Julian, 1994: Observations of the 40–50-day tropical oscillation—A review. *Mon. Wea. Rev.,* **122,** 814–837.

Maloney, E. D., and J. T. Kiehl, 2002: MJO-related SST variations over the tropical eastern Pacific during Northern Hemisphere summer. *J. Climate,* **15,** 675–689.

——, and J. Shaman, 2008: Intraseasonal variability of the West African monsoon and Atlantic ITCZ. *J. Climate,* **21,** 2898–2918.

Mathon, V., H. Laurent, and T. Lebel, 2002: Mesoscale convective system rainfall in the Sahel. *J. Appl. Meteor.,* **41,** 1081–1092.

Matsuno, T., 1966: Quasi-geostrophic motions in the equatorial area. *J. Meteor. Soc. Japan,* **44,** 25–43.

Matthews, A. J., 2000: Propagation mechanisms for the Madden-Julian oscillation. *Quart. J. Roy. Meteor. Soc.,* **126,** 2637–2652.

——, 2004a: Intraseasonal variability over tropical Africa during northern summer. *J. Climate,* **17,** 2427–2440.

——, 2004b: Atmospheric response to observed intraseasonal tropical sea surface temperature anomalies. *Geophys. Res. Lett.,* **31,** L14107, doi:10.1029/2004GL020474.

——, J. M. Slingo, B. J. Hoskins, and P. M. Inness, 1999: Fast and slow Kelvin waves in the Madden-Julian oscillation of a GCM. *Quart. J. Roy. Meteor. Soc.,* **125,** 1473–1498.

Mounier, F., and S. Janicot, 2004: Evidence of two independent modes of convection at intraseasonal timescale in the West African summer monsoon. *Geophys. Res. Lett.,* **31,** L16116, doi:10.1029/2004GL020665.

——, G. N. Kiladis, and S. Janicot, 2007: Analysis of the dominant mode of convectively coupled Kelvin waves in the West African monsoon. *J. Climate,* **20,** 1487–1503.

——, S. Janicot, and G. N. Kiladis, 2008: The West African monsoon dynamics. Part III: The quasi-biweekly zonal dipole. *J. Climate,* **21,** 1911–1928.

North, G. R., T. L. Bell, R. F. Cahalan, and F. J. Moeng, 1982: Sampling errors in the estimation of empirical orthogonal functions. *Mon. Wea. Rev.,* **110,** 699–706.

Osborne, T. M., D. M. Lawrence, J. M. Slingo, A. J. Challinor, and T. R. Wheeler, 2004: Influence of vegetation on the local climate and hydrology in the tropics: Sensitivity to soil parameters. *Climate Dyn.,* **23,** 45–61.

Reynolds, R. W., N. A. Rayner, T. M. Smith, D. C. Stokes, and W. Wang, 2002: An improved in situ satellite SST analysis for climate. *J. Climate,* **15,** 1609–1625.

Richman, M. B., 1986: Rotation of principal components. *J. Climatol.,* **6,** 293–335.

Rowell, D. P., C. K. Folland, K. Maskell, and M. N. Ward, 1995: Variability of summer rainfall over tropical North Africa (1906–92): Observations and modelling. *Quart. J. Roy. Meteor. Soc.,* **121,** 669–704.

Shinoda, T., H. H. Hendon, and J. Glick, 1998: Intraseasonal variability of surface fluxes and sea surface temperature in the tropical western Pacific and Indian Oceans. *J. Climate,* **11,** 1685–1702.

Slingo, J. M., and Coauthors, 1996: Intraseasonal oscillations in 15 atmospheric general circulation models: Results from AMIP diagnostic subproject. *Climate Dyn.,* **12,** 325–357.

Sperber, K. R., and T. N. Palmer, 1996: Interannual tropical rainfall variability in global circulation model simulations associated with the atmospheric model intercomparison project. *J. Climate,* **9,** 2727–2749.

——, J. M. Slingo, P. M. Inness, and W. K.-M. Lau, 1997: On the maintenance and initiation of the intraseasonal oscillation in the NCEP/NCAR reanalysis and in the GLA and UKMO AMIP simulations. *Climate Dyn.,* **13,** 769–795.

Sultan, B., S. Janicot, and A. Diedhiou, 2003: The West African monsoon dynamics. Part I: Documentation of intraseasonal variability. *J. Climate,* **16,** 3389–3406.

Taylor, C. M., F. Said, and T. Lebel, 1997: Interactions between the land surface and mesoscale rainfall variability during HAPEX-Sahel. *Mon. Wea. Rev.,* **125,** 2211–2227.

Thorncroft, C. D., and Coauthors, 2003: The JET2000 project—Aircraft observations of the African easterly jet and African easterly waves. *Bull. Amer. Meteor. Soc.,* **84,** 337–351.

Wheeler, M. C., and H. H. Hendon, 2004: An all-season real-time multivariate MJO index: Development of an index for monitoring and prediction. *Mon. Wea. Rev.,* **132,** 1917–1932.

——, G. N. Kiladis, and P. J. Webster, 2000: Large-scale dynamical fields associated with convectively coupled equatorial waves. *J. Atmos. Sci.,* **57,** 613–640.

Wilks, D. S., 1995: *Statistical Methods in the Atmospheric Sciences.* Academic Press, 467 pp.

Woolnough, S. J., J. M. Slingo, and B. J. Hoskins, 2000: The relationship between convection and sea surface temperature on intraseasonal timescales. *J. Climate,* **13,** 2086–2104.

——, ——, and ——, 2001: The organisation of tropical convection by intraseasonal sea surface temperature anomalies. *Quart. J. Roy. Meteor. Soc.,* **127,** 887–907.

Zhang, C., 2005: Madden-Julian oscillation. *Rev. Geophys.,* **43,** RG2003, doi:10.1029/2004RG000158.